

## REFERENCES AND NOTES

- M. Ringbauer et al., *Nat. Phys.* **11**, 249–254 (2015).
- S. Garnerone, P. Zanardi, D. A. Lidar, *Phys. Rev. Lett.* **108**, 230506 (2012).
- T. Calarco, P. Grangier, A. Wallraff, P. Zoller, *Nat. Phys.* **4**, 2–3 (2008).
- B. Sanguinetti, A. Martin, H. Zbinden, N. Gisin, *Phys. Rev. X* **4**, 031056 (2014).
- See, for example, [www.idquantique.com/random-number-generators/products/quantis-usb.html](http://www.idquantique.com/random-number-generators/products/quantis-usb.html).
- H.-K. Lo, M. Curty, K. Tamaki, *Nat. Photonics* **8**, 595–604 (2014).
- N. Walenta et al., *New J. Phys.* **16**, 013047 (2014).
- S. Nauerth et al., *Nat. Photonics* **7**, 382–386 (2013).
- U. Vazirani, T. Vidick, *Phys. Rev. Lett.* **113**, 140501 (2014).
- I. Ali-Khan, C. J. Broadbent, J. C. Howell, *Phys. Rev. Lett.* **98**, 060503 (2007).
- T. Zhong et al., *New J. Phys.* **17**, 022002 (2015).
- H. J. Kimble, *Nature* **453**, 1023–1030 (2008).
- N. Sangouard, C. Simon, H. de Riedmatten, N. Gisin, *Rev. Mod. Phys.* **83**, 33–80 (2011).
- V. Giovannetti, S. Lloyd, L. Maccone, *Nat. Photonics* **5**, 222–229 (2011).
- R. Demkowicz-Dobrzański, L. Maccone, *Phys. Rev. Lett.* **113**, 250801 (2014).
- N. Chaves, J. B. Brask, M. Markiewicz, J. Kołodziejczyk, A. Acín, *Phys. Rev. Lett.* **111**, 120401 (2013).
- H. Grote et al., *Phys. Rev. Lett.* **110**, 181101 (2013).
- M. G. Genoni, S. Olivares, M. G. A. Paris, *Phys. Rev. Lett.* **106**, 153603 (2011).
- M. D. Vidrighin et al., *Nat. Commun.* **5**, 3532 (2014).
- P. C. Humphreys, M. Barbieri, A. Datta, I. A. Walmsley, *Phys. Rev. Lett.* **111**, 070403 (2013).
- Y.-L. Zhang, H. Wang, L. Jing, L. Z. Mu, H. Fan, *Sci. Rep.* **4**, 7390 (2014).
- M. Lang, C. Caves, *Phys. Rev. A* **90**, 025802 (2014).
- P. Kok et al., *Rev. Mod. Phys.* **79**, 135–174 (2007).
- S. Aaronson, A. Arkhipov, in *Proceedings of the 43rd Annual ACM Symposium on Theory of Computing* (Association for Computing Machinery, New York, 2011), pp. 333–342.
- J. B. Spring et al., *Science* **339**, 798–801 (2013).
- M. A. Broome et al., *Science* **339**, 794–798 (2013).
- M. Tillman et al., *Nat. Photonics* **7**, 540–544 (2013).
- A. Crespi et al., *Nat. Photonics* **7**, 545–549 (2013).
- C. L. Salter et al., *Nature* **465**, 594–597 (2010).
- J. B. Spring et al., *Opt. Express* **21**, 13522–13532 (2013).
- M. Förtsch et al., *Nat. Commun.* **4**, 1818 (2013).
- F. Boitier et al., *Phys. Rev. Lett.* **112**, 183901 (2014).
- D. E. Chang, V. Vuletic, M. D. Lukin, *Nat. Photonics* **8**, 685–694 (2014).
- J. Nunn et al., *Phys. Rev. Lett.* **110**, 133601 (2013).
- H. P. Specht et al., *Nature* **473**, 190–193 (2011).
- Y. O. Dudin, L. Li, A. Kuzmich, *Phys. Rev. A* **87**, 031801(R) (2013).
- D. G. England, P. J. Bustard, J. Nunn, R. Lausten, B. J. Sussman, *Phys. Rev. Lett.* **111**, 243601 (2013).
- D.-S. Ding, Z. Y. Zhou, B. S. Shi, G. C. Guo, *Nat. Commun.* **4**, 2527 (2013).
- W. J. Munro, K. Azuma, K. Tamaki, K. Nemoto, *IEEE J. Select. Top. Quant. Elec.* **21**, 6400813 (2015).
- W. Pfaff et al., *Science* **345**, 532–535 (2014).
- A. E. Lita, A. J. Miller, S. W. Nam, *Opt. Express* **16**, 3032–3040 (2008).
- J. J. Renema et al., *Phys. Rev. Lett.* **112**, 117604 (2014).
- F. Marsili et al., *Nat. Photonics* **7**, 210–214 (2013).
- A. Reiserer, S. Ritter, G. Rempe, *Science* **342**, 1349–1351 (2013).

## ACKNOWLEDGMENTS

I acknowledge support from the UK Engineering and Physical Sciences Research Council, the UK Quantum Technology Network, the European Commission through the Marie Curie Actions, the European Research Council, and the U.S. European Office of Aerospace Research and Development. I thank J. Nunn and W. S. Kolthammer for insightful discussions and helpful comments on the manuscript.

10.1126/science.aab0097

## REVIEW

# Beyond crystallography: Diffractive imaging using coherent x-ray light sources

Jianwei Miao,<sup>1\*</sup> Tetsuya Ishikawa,<sup>2</sup> Ian K. Robinson,<sup>3,4</sup> Margaret M. Murnane<sup>5</sup>

X-ray crystallography has been central to the development of many fields of science over the past century. It has now matured to a point that as long as good-quality crystals are available, their atomic structure can be routinely determined in three dimensions. However, many samples in physics, chemistry, materials science, nanoscience, geology, and biology are noncrystalline, and thus their three-dimensional structures are not accessible by traditional x-ray crystallography. Overcoming this hurdle has required the development of new coherent imaging methods to harness new coherent x-ray light sources. Here we review the revolutionary advances that are transforming x-ray sources and imaging in the 21st century.

The x-ray science community has witnessed two revolutionary developments over the past two decades. First, large- and small-scale coherent x-ray sources, including advanced synchrotron sources, x-ray free electron lasers (XFELs), and high harmonic generation (HHG) sources, are under rapid development worldwide (1–3). Compared with the previous generations of x-ray sources, the new light sources have remarkable properties. XFELs increase the coherent x-ray flux by nine orders of magnitude, while tabletop HHG sources generate a coherent x-ray supercontinuum that spans the entire electromagnetic spectrum from the ultraviolet (UV) to the kilo-electron volt (keV) region, covering 12 octaves of bandwidth. In addition, HHG and XFEL pulses are extremely short, ranging from tens of attoseconds to hundreds of femtoseconds. Second, a new approach to x-ray crystallography, known as coherent diffractive imaging (CDI), enables structure determination of noncrystalline specimens and nanocrystals with a resolution limited only by the spatial frequency of the diffracted waves (4). Moreover, CDI enables simultaneous amplitude and phase contrast imaging. In recent years, the combination of powerful coherent x-ray light sources and CDI methods, coupled with advanced x-ray detectors and computational algorithms, has opened up new research frontiers in the physical and biological sciences that are simply not attainable with conventional x-ray crystallography (5–19). Here, we review progress in CDI and the advanced x-ray light sources that are allowing this new imaging modality to blossom. We highlight the exciting scientific discoveries that were enabled by these new capabilities and look forward with great

anticipation to the new frontiers in imaging that are emerging.

## Coherent diffractive imaging methods

In a traditional microscope, a lens is used to collect the light scattered by a sample and thereby recover an image. However, in the x-ray region, the use of lenses introduces a severe limitation because diffractive x-ray optics must be used, and these are far from perfect. Although x-ray microscopes with ~10-nm spatial resolution have been demonstrated, ~25 nm is more typical—which is nowhere near the wavelength limit (20). CDI avoids this limitation by illuminating an object with a coherent laser-like beam and collecting the scattered light on a detector (Fig. 1, A to E). The image of the object can then be recovered with an advanced phase retrieval algorithm by taking advantage of the fact that the diffracted wave is proportional to the Fourier transform of the object (4). However, although the magnitude squared of the Fourier transform can be measured by a detector, the phase information is lost. This constitutes the well-known phase problem associated with recovering an image from a diffraction pattern. For a noncrystalline specimen, the diffraction pattern is continuous and can be sampled at a frequency finer than the Nyquist interval (the inverse of the specimen size). For a noise-free diffraction pattern, when the number of independently sampled intensity points is larger than (or equal to) the number of unknown variables associated with a specimen, the phase information is in principle encoded inside the diffraction intensity (21) and can usually be retrieved by iterative algorithms (22, 23). Furthermore, because no optics is inserted between the specimen and detector, CDI represents the most photon-efficient x-ray imaging modality (24).

By combining phase retrieval algorithms (Box 1) and coherent x-ray sources, several CDI methods have now been developed in both transmission and reflection modes, including plane-wave CDI (PCDI), Bragg CDI (BCDI), ptychographic CDI (ptychography), Fresnel CDI, reflection CDI, sparsity CDI, and others (5–18, 25, 26). Figure 1, A to

<sup>1</sup>Department of Physics and Astronomy and California NanoSystems Institute, University of California, Los Angeles, CA 90095, USA. <sup>2</sup>RIKEN SPring-8 Center, Kouto 1-1-1, Sayo, Hyogo 679-5148, Japan. <sup>3</sup>London Centre for Nanotechnology, University College London, 17-19 Gordon Street, WC1H 0AH, UK. <sup>4</sup>Research Complex at Harwell, Harwell Campus, Didcot, Oxford OX11 0DE, UK. <sup>5</sup>JILA, University of Colorado, and National Institute of Standards and Technology (NIST), Boulder, Boulder, CO 80309, USA.

\*Corresponding author. E-mail: miao@physics.ucla.edu

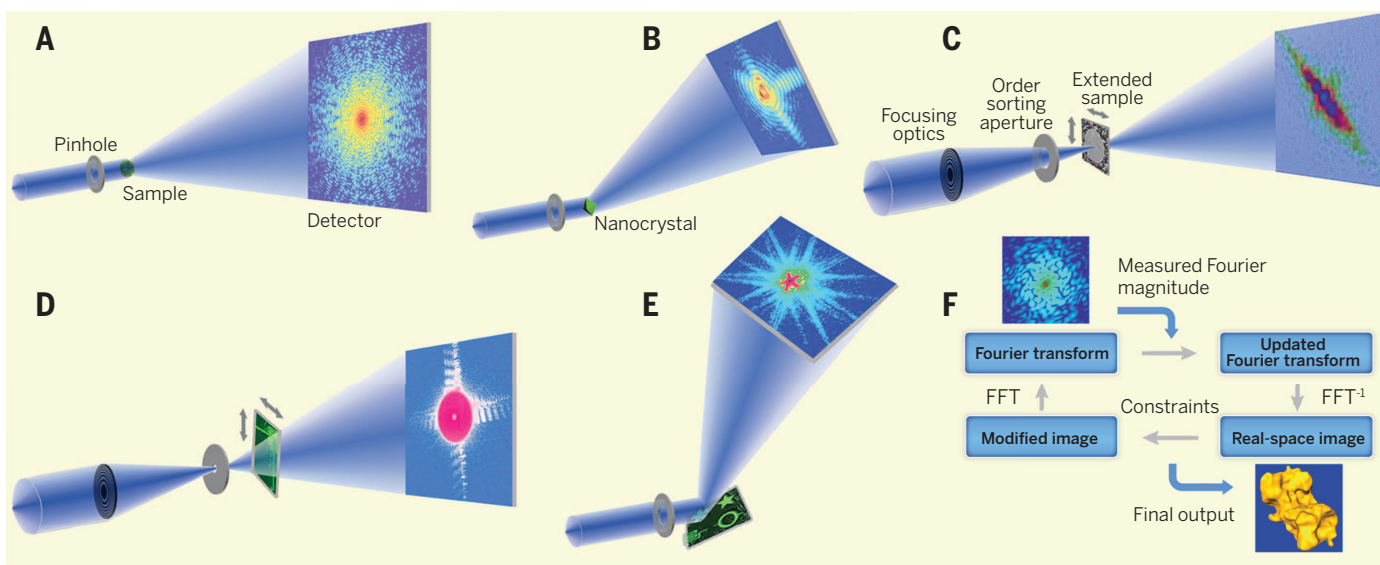


**Fig. 1. Schematic layout of five main CDI methods and iterative phase retrieval algorithms.** (A) Plane-wave CDI: A plane wave illuminates a sample, and an oversampled diffraction pattern is measured by a detector. (B) Bragg CDI: The diffraction pattern surrounding a Bragg peak is acquired from a nanocrystal. (C) Ptychographic CDI: A coherent x-ray probe is generated by an aperture or focusing optics. An extended sample is scanned through the probe on a 2D grid, and diffraction patterns are collected from a series of partially overlapping regions. (D) Fresnel CDI: A sample is positioned in front of (or behind) the focal spot of a coherent x-ray wave, and the Fresnel diffraction

pattern is measured by a detector. (E) Reflection CDI: A coherent x-ray wave is specularly reflected off a sample on a substrate, and the diffraction intensity around the reflected beam is collected by a detector. (F) Phase retrieval algorithms iterate back and forth between real and reciprocal space. In each iteration, various constraints, including support, positivity (i.e., electron density cannot be negative), or partially overlapping regions, are enforced in real space, while the measured Fourier magnitude is updated in reciprocal space. Usually, after hundreds to thousands of iterations, the correct phase information can be recovered.

E, shows the schematic layout of the five major CDI methods to date. In the original PCDI, a plane wave illuminates an object in transmission, and the diffraction pattern is measured by an area detector (Fig. 1A). To satisfy the oversampling criterion, either an isolated object or a finite illumination had to be implemented. To obtain 3D structural information, a tilt series of diffraction patterns is acquired over various sample orientations and then phased to obtain a 3D image (6, 11). Because PCDI is insensitive to sample drift and vibration, it achieved the highest 2D and 3D spatial resolution ( $\approx 2$  and  $5.5$  nm, respectively) of any x-ray imaging method (27, 28). In BCDI, a coherent beam of x-rays illuminates a nanocrystal, and the diffraction pattern surrounding a Bragg peak is measured (Fig. 1B) (5, 8). Inversion of the diffraction pattern yields a complex 3D image, whose phase is related to the displacement and strain field of the crystal lattice. Furthermore, BCDI is also useful for powder and polycrystalline samples, where many randomly oriented grains are in the beam at the same time. Because the Bragg peak of each grain will be in a different location in reciprocal space, individual grains can be isolated from their neighbors.

Ptychography brings powerful new imaging capabilities because it can image an extended sample in either reflection or transmission modes, with near-wavelength spatial resolution ( $\approx 1.3 \lambda$ ) horizontally and subnanometer (sub-nm) resolution vertically (18, 29). In ptychography, the sample is scanned on a 2D grid to collect a series of diffraction patterns from partially overlapping regions (Fig. 1C). This additional redundancy in

the diffraction data enables robust image reconstruction with quantitative phase contrast (12), while also extracting the complex x-ray illumination beam, correcting for errors in the scanning stages, and improving the convergence of the iterative phase retrieval process (13, 18). In Fresnel CDI, a sample is illuminated by a curved wavefront through defocusing of an x-ray beam, and the resulting Fresnel diffraction pattern is measured by a detector (Fig. 1D). If the incident beam is independently characterized and the geometrical dimensions of the experiment are accurately determined, the exit wave at the sample can be quantitatively reconstructed by using an iterative algorithm with fast convergence (10).

CDI has also been successfully implemented in reflection mode, giving beautiful 3D height maps of a surface, with near-wavelength transverse resolution, sub-nm vertical resolution, and very high phase and amplitude contrast due to the short wavelength of the illumination light (18, 26, 30, 31). Moreover, the geometry is very simple: A coherent x-ray beam illuminates a sample, and the diffracted light can then be collected with very high numerical aperture (Fig. 1E). When combined with powerful ptychographic imaging, high-quality images of extended samples can be obtained (18). Reflection CDI is complementary to other imaging modalities, such as scanning electron microscopy (SEM) and atomic force

### Box 1. Iterative phase retrieval algorithms.

A common feature of these algorithms requires iterating between real and reciprocal space (23), consisting of the following four steps in each iteration (Fig. 1F): (i) The algorithms usually start with a random phase set as the initial guess. By combining this random phase set with the measured Fourier magnitude and then applying an inverse fast Fourier transform (FFT), an initial image is computed; (ii) depending on oversampling of the diffraction intensity, a support (i.e., a boundary slightly larger than the sample envelope) can be estimated from the image. The electron density outside the support of the image is reduced, while the negative electron density inside the support is modified—for example, by setting to zero, depending on the algorithm; (iii) by applying a FFT to the updated image, a new Fourier transform is generated; and (iv) by replacing its magnitude with the measured data, a better estimate of the Fourier transform is obtained and used for the next iteration. This process is then repeated, and each iteration is characterized by an error metric, defined as the difference between the calculated and measured Fourier magnitudes. Usually, after hundreds to thousands of iterations, the correct phase set can be retrieved.

microcopy (AFM), allowing for long (>3 cm) working distances, less damage, and higher-contrast imaging than other approaches.

### A revolution in coherent x-ray light sources

In the past decade, there has also been a revolution in the development of both large-scale and tabletop coherent x-ray sources (Fig. 2). Large-scale x-ray sources are based on high-energy accelerators, which emit x-rays with varying degrees of coherence (23). When the first so-called third-generation x-ray synchrotron facilities were designed, it was widely believed that undulators for hard x-rays would require high-energy electron beams. As a result, the first third-generation facilities used electron storage rings with energies of 6 to 8 GeV and low-emittance electron beams to enhance the brightness of the undulator radiation (23). However, despite their small source size and long source-sample distance, these third-generation facilities radiated only a small amount of spatially coherent light ( $\approx 0.1\%$  of total). Nevertheless, by using a small aperture, this small fraction of spatially coherent light could be extracted and used to perform the first CDI experiment at the National Synchrotron Light Source (4). A maturation of undulator technology enabled the development of higher harmonics and shorter-period undulators, which can produce hard x-rays without requiring high-energy storage rings. Thus, lower energy ( $\sim 3$  GeV), medium-sized storage rings are now used for hard x-ray sources where a wide variety of CDI activities are now in progress. Another new and important trend of accelerator-based advanced x-ray sources is the use of a new magnetic lattice, known as a multi-bend-achromat, to more tightly focus the electron

beam, further reduce its emittance, and increase the x-ray brilliance (23).

At the turn of the 21st century, brighter XFEL sources were developed (23) based on self-amplified spontaneous emission (SASE) (Fig. 2A, inset) (1, 2). When a low-emittance, high-density, and high-energy electron bunch is injected into a long undulator ( $\sim 100$  m), it initially emits synchrotron radiation. The emitted photons travel at the speed of the light inside the undulator, which is only slightly faster than the velocity of the high-energy electron bunch. As a result, the radiation interacts back with the electron bunch. If the undulator is designed such that the interaction makes the faster electrons slower and slower electrons faster, the electron bunch density is periodically modulated by the radiation, a process called microbunching. The process exponentially increases the intensity of the emitted radiation, as well as the interaction between the radiation and the electron bunch, introducing “gain” in a manner similar to that of a conventional laser. At the end of the long undulator, the gain is saturated and an extremely intense XFEL pulse is produced. The peak brightness of the XFEL pulse is  $10^9$  times higher than that of the most powerful third-generation source (Fig. 2A), while their pulse duration ranges from tens to hundreds of femtoseconds, although with lower repetition rate and some timing jitter.

In parallel with advances in large-scale coherent x-ray facilities, the same revolution that visible lasers underwent in the 1960s is now happening for tabletop coherent x-ray sources. Interestingly, the first tabletop-scale coherent soft x-ray source was not based on creating a population inversion to support laser action, but was rather based on nonlinear optics. In nonlinear optics, the high

electric fields that are present in a focused laser beam can drive electrons in a highly irregular (anharmonic) motion that reradiates harmonics of the driving laser light at much shorter wavelengths. In HHG, the laser field intensity must be sufficient to tunnel ionize the atoms used as the nonlinear medium, by suppressing the Coulomb field that normally binds the electron to the ion. For the few-femtosecond time interval during which this is happening, the laser-driven quantum wave function of the electron can radiate coherent high-harmonic x-rays. If x-rays from a macroscopic number of atoms interfere constructively to generate a laser-like beam, in a process called phase matching, HHG can have spectacular temporal and spatial coherence. This is because of the ultra-precise timing relationship between the laser and x-ray fields that are synchronized to less than 1 attosecond.

Although its physical manifestation is very different, HHG can also be thought of as a coherent laser-driven version of the Röntgen x-ray tube. However, the full power of femtosecond lasers for manipulating the quantum wave function of an electron is now being realized. By changing the color and polarization of the driving laser, the HHG spectrum, pulse duration, and polarization can be controlled (3, 32, 33), thus making it possible to generate x-ray bursts with durations from tens of attoseconds to tens of femtoseconds, with a coherent bandwidth spanning 12 octaves, from  $<100$  meV to  $\approx 1$  keV. One recent surprising finding is that longer-wavelength mid-infrared lasers can generate shorter-wavelength bright x-ray beams. Using  $4\text{-}\mu\text{m}$  driving lasers, for example, HHG emerges as a broad coherent supercontinuum, spanning the entire electromagnetic spectrum from the ultraviolet to the soft x-ray keV region of

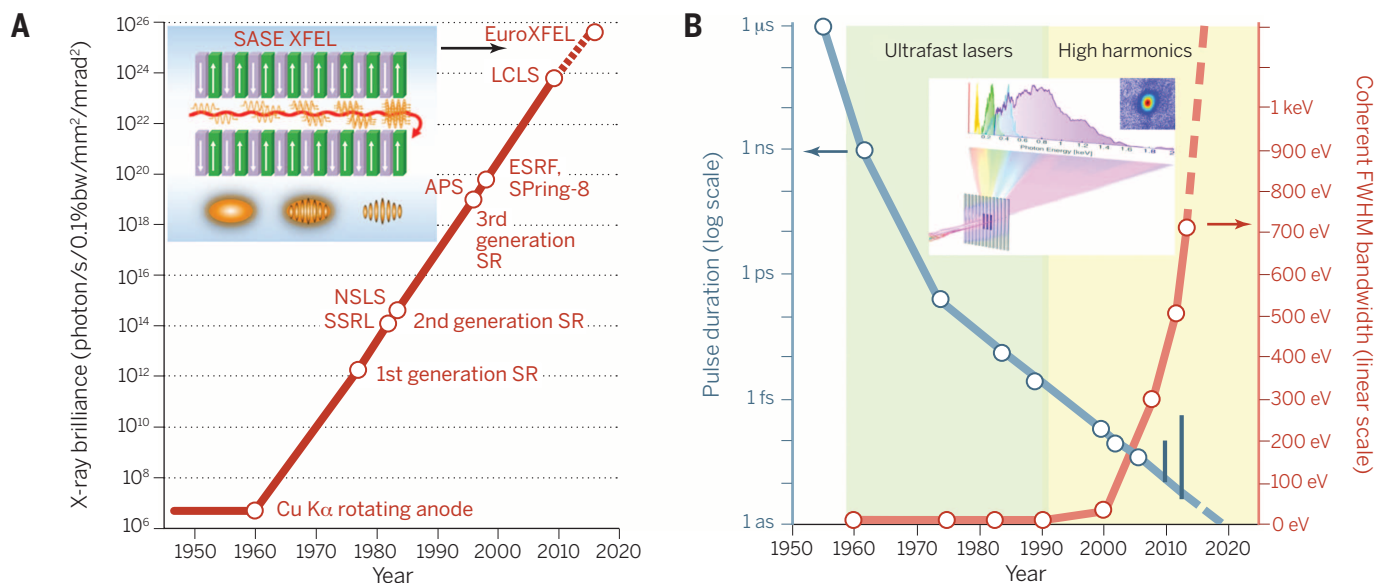


**Fig. 2. Revolution in coherent x-ray sources.** (A) The x-ray brilliance of coherent light sources has improved by 20 orders of magnitude in 6 decades (brilliance is a measure of coherent x-ray flux). The inset shows the SASE process to produce extremely intense and ultrashort XFEL pulses. (B) Progress in tabletop coherent bandwidth and pulse duration as a function of year. Coherent high harmonics can generate an x-ray supercontinuum or a series of narrowband peaks spanning the UV to the keV region, supporting the shortest bursts of light to date. The vertical lines show both the transform-limited pulse duration and the chirped isolated bursts that emerge when HHG is driven by infrared lasers. The inset shows the HHG spectrum and laser-like beam. FWHM, full width at half maximum.

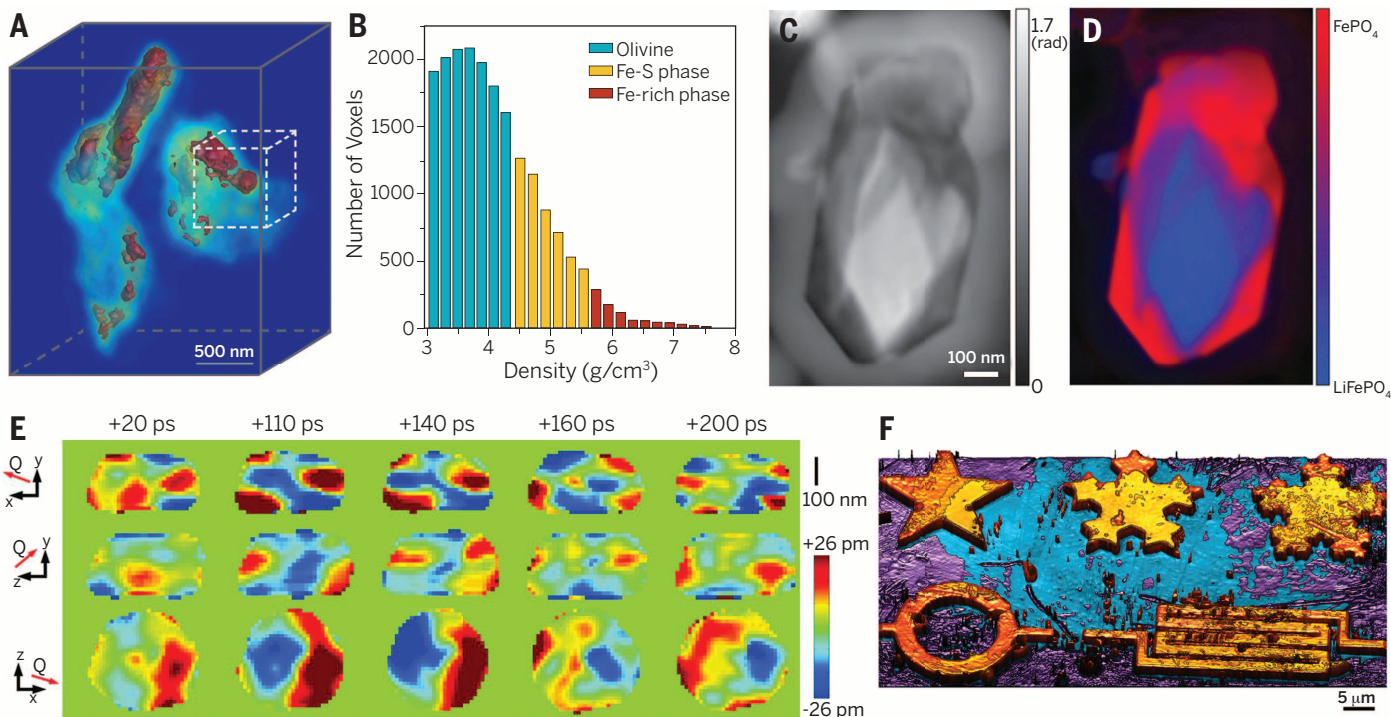


**Fig. 3. Physical science applications of diffractive imaging methods with coherent x-rays.** (A) 3D morphology of Fe-rich and Fe-S phases in an olivine matrix (37). (B) Histogram of the Fe-rich phase, Fe-S phase, and olivine distribution within a dotted-line cube in (A). (C) Phase of the ptychographic reconstruction of a partially delithiated nanoplate of  $\text{LiFePO}_4$  (40). (D) Chemical composition image of the nanoplate showing the distribution of two chemical species:  $\text{LiFePO}_4$

and  $\text{FePO}_4$ . (E) 3D imaging of lattice dynamics in a gold nanocrystal (17). Orthogonal cut through the center of the nanocrystal showing the displacement as a function of delay time at three different directions. The  $\mathbf{Q}$  vector represents the direction of the displacement field. (F) 3D profile of a ptychographic reconstruction with spatial resolution of  $<1.3 \lambda$  horizontally and sub-nm vertically, which was acquired by using a tabletop HHG source with  $<1$ -min exposure time (18).

the spectrum to wavelengths  $<8 \text{ \AA}$ . Moreover, these x-rays emerge as isolated attosecond bursts, which are predicted to scale to the subattosecond (i.e., zeptosecond) regime with longer-wavelength lasers (33). In contrast, using intense UV driving lasers, HHG emerges as a series of bright narrow-band peaks, with  $\approx 10$ -fs pulse duration. Finally, by manipulating the electron wave function with bichromatic (two-color) circularly polarized counter-rotating laser beams, it is now possible to produce bright circularly polarized harmonics that complement the bright linearly polarized HHG beams that have been available for 20 years (32).

The powerful quantum coherence of HHG makes it ideal for imaging the fastest dynamics relevant to function in atoms, molecules, nano-systems, and materials, at multiple atomic sites simultaneously. HHG is complementary to the powerful XFEL machines, because it can be driven by a small-scale ( $\approx \text{mJ}$  energy) laser at very high repetition rates (1 to 100 kHz). Although the pulse energies are lower than those available at XFELs (nJ versus mJ), the repetition rates are higher and are ideal for several exciting applications discussed below (3, 32–36).

#### Multidisciplinary science enabled by coherent x-ray light sources and diffractive imaging

CDI is ideally suited for quantitative 3D characterization of materials at the nanoscale: X-rays have a larger penetration depth than electrons,

so that destructive sample preparation can often be avoided. Moreover, by quantifying the incident and diffracted x-ray flux, CDI can extract the mass density and thus distinguish different phases in materials in three dimensions (37). Furthermore, the presence of core shell x-ray absorption provides chemical contrast, while their polarization can be exploited to provide magnetic contrast and molecular orientation. Thus, CDI enables nanoscale chemical, elemental, and magnetic mapping of complex matter (38–40). Finally, the high temporal resolution of the new coherent x-ray sources such as HHG and XFELs already make it possible to capture the fastest charge, spin, and lattice motions in matter, on multiple length and time scales.

In recent work, PCDI was used to quantitatively image a molten Fe-rich alloy and crystalline olivine sample, which was synthesized at 6 GPa and  $1800^\circ\text{C}$  to mimic the conditions of Earth's upper mantle (37). Figure 3A shows the 3D morphology of the Fe-rich and Fe-S phases in an olivine matrix in which the molten Fe exhibits varied shapes and sizes. A histogram of the 3D mass density distribution of the sample indicates that the Fe-rich and Fe-S phases change continuously instead of abruptly (Fig. 3B)—owing to local temperature, pressure, geometry, and microscopic percolation mechanisms, which are difficult to probe with other imaging techniques.

In other exciting developments, Fig. 3C shows a ptychographic image of a partially delithiated nanoplate of  $\text{LiFePO}_4$ , a material with broad po-

tential application in electrochemical energy storage (40). By acquiring multiple images across the Fe L-shell x-ray absorption edge and using them as input to principal-component and singular-value decomposition analysis, a chemical composition image of the partially delithiated nanoplate is obtained, showing the distribution of two chemical species:  $\text{LiFePO}_4$  and  $\text{FePO}_4$  (Fig. 3D). The resolution of this chemical image ( $\sim 18 \text{ nm}$ ) is nearly an order of magnitude higher than the probe size (150 nm) and more than three times better than that of state-of-the-art scanning transmission x-ray microscopy (20). These results suggest that the (de)lithiation reaction of  $\text{LiFePO}_4$  is two-phase, where both phases coexist in these submicrometer nanoplates.

BCDI's unique ability to image displacement (strain) fields in 3D also has widespread applications in materials science and nanoscience. For example, it was used to understand the structural principles of metal nanoparticles (5, 8) and to obtain quantitative 3D images of the full strain tensor when the projections from three or more noncoplanar Bragg peaks are combined to yield the full vectorial displacement field (41). XFELs also provide sufficient coherent x-ray flux in a single monochromatic femtosecond pulse to record a slice through the BCDI diffraction pattern of a nanocrystal. A pump-probe BCDI experiment was carried out on 300-nm-diameter Au nanocrystals (17). The nanocrystals were first excited by an 800-nm Ti-sapphire infrared laser pulse

and then followed by snapshot imaging of the excited state with XFEL BCDI. Provided that both laser and x-ray pulses were kept below their damage thresholds, full 3D diffraction patterns could be built up as a function of delay time from the same nanocrystal. In this way, movies were captured of the strain associated with whole-crystal vibrations, with a 200-ps period (Fig. 3E). Two simple dilation breathing modes and a previously unknown shear mode were identified (17).

Using tabletop HHG, full-field coherent imaging in both reflection and transmission geometries has been demonstrated, with record spatial resolution of 22 nm (transverse) and 6 Å (axial) (18, 42). Figure 3F shows aptychographic image of a surface, with spatial resolution  $<1.3\lambda$  or 40 nm horizontally, 6 Å vertically, and acquired with  $<1$  min of x-ray exposure time (18). Moreover, the phase contrast in CDI is enhanced owing to the use of extreme ultraviolet ( $\lambda = 30$  nm) illumination. Compared with SEM or AFM, HHG-based CDI enables higher-contrast full-field imaging with less sample damage, with long working distances ( $\approx 3$  to 10 cm), automatic correction for imperfect scanning stages, and femtosecond time resolution ( $\approx 10$  fs).

Several discoveries have been made recently simply by monitoring the time-dependent HHG diffraction from a material after excitation by a laser pulse, to uncover which mechanisms are responsible for nanoscale energy, charge, and spin transport (19, 35). One remarkable demonstration of this capability showed that the cooling rate for a nanometer-size heat source depends on its proximity to other sources, cooling more rapidly when spaced close together than when isolated. This finding represents fundamentally new materials science directly relevant to the design of future energy-efficient nanosystems (19, 36). Real-time imaging in 3D through opaque materials will represent a powerful capability for understanding functional nanosystems.

For biological applications, CDI is complementary to optical and electron microscopies in terms of spatial resolution, sample thickness, contrast mechanism, and quantitative capability. By using novel imaging technologies and labeling techniques, superresolution fluorescence microscopy can study dynamic processes in living cells at the tens-of-nanometers level, but it requires labeling of specific molecules and can accommodate limited sample thickness. To achieve considerably higher resolu-

tion, electron microscopy is the method of choice, but it is limited to imaging thinner samples, owing to the short penetration depth of electrons. Compared with superresolution and electron microscopy, CDI has three distinctive features. First, because of the large penetration depth of x-rays, CDI can image whole biological cells without the need of sectioning. Second, CDI takes advantage of the phase shift (contrast) of the intrinsic density of biological specimens that enables quantitative 3D imaging of the entire contents of cells and cellular organelles by using their natural contrast. Finally, by avoiding the use of lenses, the resolution of CDI is limited only by the spatial frequency of the diffracted waves from the sample.

Using third-generation synchrotrons, CDI has been used to image whole cells, cellular organelles, viruses, and biological materials, with spatial resolution down to  $\sim 11$  nm (7, 43–48). As an example, Fig. 4A shows the 3D mass density distribution of a whole, unstained yeast spore cell in which the 3D structure of intercellular organelles is quantitatively identified (44). Figure 4, B and C, shows the 3D image of an unstained human chromosome, as well as the first coherent diffraction pattern ever measured from a single, unstained

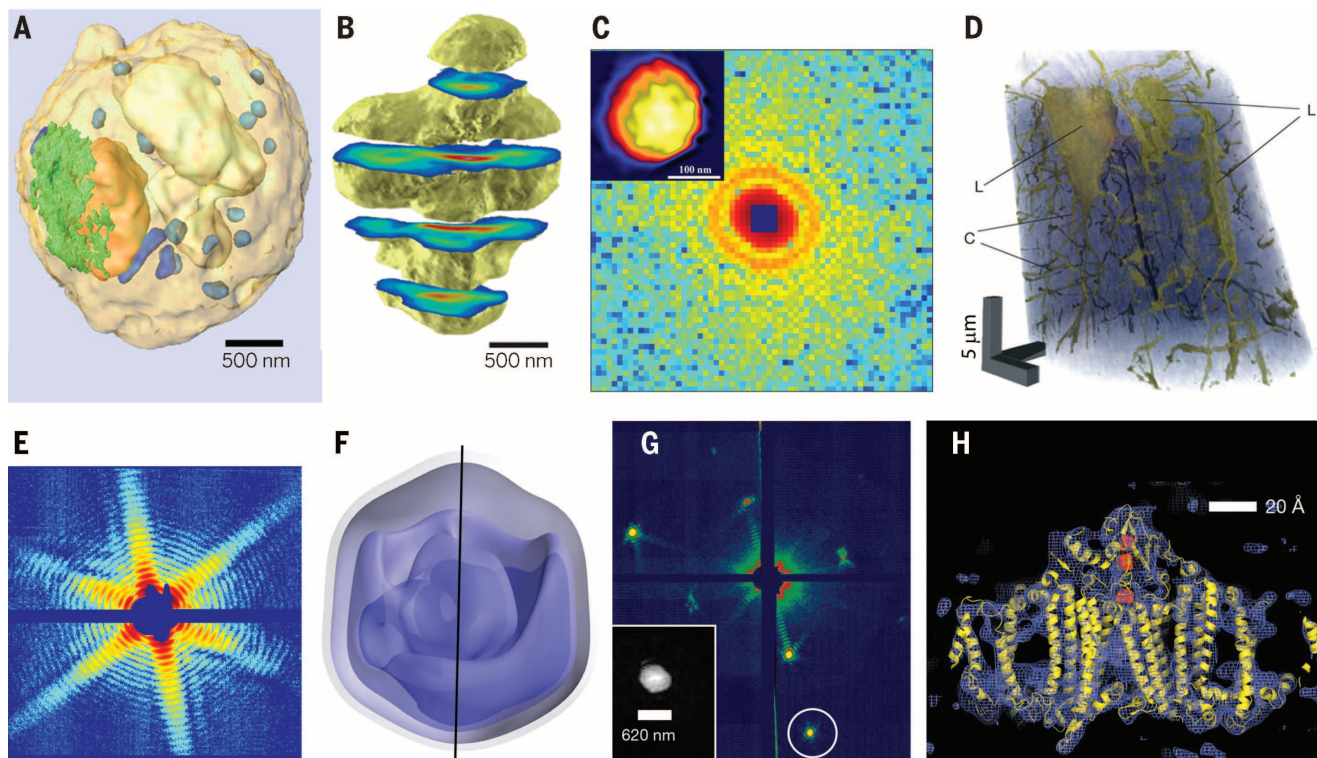


**Fig. 4. Biological applications of diffractive imaging methods with coherent x-rays.** (A) 3D mass density distribution of a whole, unstained yeast spore cell, showing nucleus (orange), endoplasmic reticulum (green), vacuole (white), mitochondria (blue), and granules (light blue) (44). (B) 3D image of an unstained human chromosome where the highest electron density is around the centromere (in red) (46). (C) First coherent x-ray diffraction pattern measured from a single, unstained herpesvirus virion and its reconstructed structure (inset), where the capsid is in yellow (47). (D) Quantitative 3D measurements of the osteocyte lacunae (L) and the connecting canaliculi (C) in a bone matrix (15). (E) A representative diffraction pattern of a giant mimivirus particle collected with a single

LCLS pulse, where the symmetry of the diffraction pattern is clearly visible (16). (F) 3D structure of the mimivirus reconstructed from 198 diffraction patterns with higher density in blue and lower density in white (50). The vertical line represents the pseudo-fivefold axis. (G) Coherent x-ray diffraction pattern collected from a photosystem I nanocrystal using the LCLS, where the interference pattern between the Bragg peaks is visible owing to the finite size of the nanocrystal (54). (Inset) Real-space image of the nanocrystal reconstructed from the circled Bragg shape transform. (H)  $2mF_o - DF_c$  electron density map at  $1.0\sigma$  (purple mesh), obtained from diffraction intensities with more than 15,000 photosystem I nanocrystals (the refined model shown in yellow).

virus particle and its reconstructed structure (46, 47). CDI has also been applied to study biological composite materials, including nanoscale imaging of mineral crystals in bone at different stages of mineralization (48) and quantitative 3D measurements of the osteocyte lacunae and the connecting canaliculi in a bone matrix (Fig. 4D) (15).

Using XFELs, CDI has been applied to measure the diffraction patterns of biological samples with single extremely intense and short x-ray pulses before the onset of radiation damage (diffraction-before-destruction) (9, 49). Two important directions have been pursued. One is to perform diffractive imaging of live cells, cellular organelles, and virus particles with a resolution down to ~18 nm (16, 50–53), which is presently limited by the x-ray flux density on the sample. Figure 4E shows a representative diffraction pattern of a giant mimivirus particle measured with a single Linac Coherent Light Source (LCLS) pulse (16). Using 198 diffraction patterns, the 3D structure of the mimivirus was reconstructed, revealing a nonuniform internal structure (Fig. 4F) (50). The other uses nanometer- to micrometer-sized protein crystals to substantially increase the resolution of diffraction patterns from single XFEL pulses (Fig. 4, G and H) (54). This method, known as serial femtosecond crystallography, has achieved a highest resolution of 1.6 Å (55) and also been applied to the structure determination of proteins that are difficult to grow as large crystals, such as membrane proteins (56, 57).

## Looking forward

Looking into the future for this 2015 Year of Light, we can already identify three research frontiers in imaging science and applications using small and large-scale coherent x-ray light sources. First, by taking advantage of the extremely short XFEL and HHG pulses, CDI is ideally suited to probe functioning systems at the nanoscale—at multiple sites simultaneously. A new form of CDI—hyperspectral imaging based on ptychography (12)—makes it possible to retrieve an image at several different x-ray wavelengths simultaneously, encoding instantaneous charge and spin information. Recently, dynamic CDI has been applied to image coherent acoustic phonons in nanocrystals, nanofabricated structures undergoing laser ablation, and standing surface acoustic waves in a piezoelectric substrate with spatial resolutions of tens of nanometers and temporal resolutions of picoseconds to <10 fs (17, 34, 35, 58, 59). With further improvement in experimental design, dynamic CDI should be able to achieve spatial resolutions <10 nm and temporal resolutions of 10 fs. Such a powerful imaging technique with high spatial-temporal resolutions is expected to profoundly expand our understanding of a wide range of dynamic phenomena, ranging from phase transitions, charge transfer, transport, nucleation, melting, superheating, crack and shock formation to lattice and grain boundary dynamics, as well as materials discovery of transient “hidden” phases of matter.

Second, as the wavelength of x-rays is on the order of the size of an atom, scientists have long

dreamed of the development of atomic-resolution x-ray microscopy. However, the highest resolution presently attainable by any x-ray imaging method is ~2 nm in 2D and ~5.5 nm in 3D (27, 28). With the rapid development of coherent light sources that promise to increase the x-ray brilliance by several orders of magnitude (Fig. 2A), CDI may achieve atomic resolution for radiation hard samples. Although electron microscopy can routinely image crystalline materials at atomic resolution, x-rays have several distinctive properties compared to electrons: (i) X-rays interact with the electron density rather than the Coulomb potential of an atom; (ii) dynamical scattering is usually negligible, allowing study of thick specimens; and (iii) the sample can be placed in an ambient environment. Thus, the potential ability to achieve atomic-resolution CDI, coupled with elemental, chemical, and magnetic specificity, would find broad applications in both fundamental and applied science.

Finally, one of the ultimate goals of CDI is to achieve high-resolution single-particle imaging (SPI)—for example, of protein complexes—without the need of crystallization. Using extremely intense and ultrashort XFEL pulses, coherent x-ray diffraction patterns can be collected from single protein complexes based on the diffraction-before-destruction scheme (49). These diffraction patterns can then be assembled into 3D patterns from which a 3D image follows after inversion (60–62). Numerical simulations show that with ~10<sup>5</sup> to 10<sup>6</sup> identical copies of large protein molecules, the 3D structure of the molecules can be determined at near-atomic resolution (60). Recent XFEL experiments have demonstrated the feasibility of the SPI method but at much lower resolution (16, 50–53). To improve the spatial resolution, the XFEL pulse intensity has to be increased by two to three orders of magnitude. Recent work has suggested that the combination of self-seeding (using x-rays from the first half of the undulator to seed the second half via a monochromator) and undulator tapering (a gradual reduction in the field strength of an undulator to preserve the resonance wavelength) can achieve a 100-fold increase of the XFEL peak power (23). The increase in the XFEL pulse flux, coupled with large dynamic-range detectors, could realize the potential of SPI at higher resolution.

## REFERENCES AND NOTES

1. P. Emma *et al.*, *Nat. Photonics* **4**, 641–647 (2010).
2. T. Ishikawa *et al.*, *Nat. Photonics* **6**, 540–544 (2012).
3. T. Popmintchev *et al.*, *Science* **336**, 1287–1291 (2012).
4. J. Miao, P. Charalambous, J. Kirz, D. Sayre, *Nature* **400**, 342–344 (1999).
5. I. K. Robinson, I. A. Vartanyants, G. J. Williams, M. A. Pfeifer, J. A. Pitney, *Phys. Rev. Lett.* **87**, 195505 (2001).
6. J. Miao *et al.*, *Phys. Rev. Lett.* **89**, 088303 (2002).
7. J. Miao *et al.*, *Proc. Natl. Acad. Sci. U.S.A.* **100**, 110–112 (2003).
8. M. A. Pfeifer, G. J. Williams, I. A. Vartanyants, R. Harder, I. K. Robinson, *Nature* **442**, 63–66 (2006).
9. H. N. Chapman *et al.*, *Nat. Phys.* **2**, 839–843 (2006).
10. G. J. Williams *et al.*, *Phys. Rev. Lett.* **97**, 025506 (2006).
11. H. N. Chapman *et al.*, *J. Opt. Soc. Am. A Opt. Image Sci. Vis.* **23**, 1179–1200 (2006).
12. J. M. Rodenburg *et al.*, *Phys. Rev. Lett.* **98**, 034801 (2007).
13. P. Thibault *et al.*, *Science* **321**, 379–382 (2008).
14. K. S. Raines *et al.*, *Nature* **463**, 214–217 (2010).
15. M. Dierolf *et al.*, *Nature* **467**, 436–439 (2010).

16. M. M. Seibert *et al.*, *Nature* **470**, 78–81 (2011).
17. J. N. Clark *et al.*, *Science* **341**, 56–59 (2013).
18. M. D. Seaberg *et al.*, *Optica* **1**, 39–44 (2014).
19. M. E. Siemens *et al.*, *Nat. Mater.* **9**, 26–30 (2010).
20. A. Sakdinawat, D. Attwood, *Nat. Photonics* **4**, 840–848 (2010).
21. J. Miao, D. Sayre, H. N. Chapman, *J. Opt. Soc. Am. A Opt. Image Sci. Vis.* **15**, 1662–1669 (1998).
22. J. R. Fienup, *Opt. Lett.* **3**, 27–29 (1978).
23. See supplementary text in supplementary materials on Science Online.
24. X. Huang *et al.*, *Opt. Express* **17**, 13541–13553 (2009).
25. A. Szameit *et al.*, *Nat. Mater.* **11**, 455–459 (2012).
26. T. Sun, Z. Jiang, J. Strzalka, L. Ocola, J. Wang, *Nat. Photonics* **6**, 586–590 (2012).
27. Y. Takahashi *et al.*, *Phys. Rev. B* **82**, 214102 (2010).
28. R. Xu *et al.*, *Nat. Commun.* **5**, 4061 (2014).
29. A. M. Maiden, J. M. Rodenburg, *Ultramicroscopy* **109**, 1256–1262 (2009).
30. I. K. Robinson *et al.*, *Phys. Rev. B* **60**, 9965–9972 (1999).
31. S. Roy *et al.*, *Nat. Photonics* **5**, 243–245 (2011).
32. O. Kfir *et al.*, *Nat. Photonics* **9**, 99–105 (2015).
33. C. Hernández-García *et al.*, *Phys. Rev. Lett.* **111**, 033002 (2013).
34. E. Turgut *et al.*, *Phys. Rev. Lett.* **110**, 197201 (2013).
35. D. Rudolf *et al.*, *Nat. Commun.* **3**, 1037 (2012).
36. K. M. Hoogeboom-Pot *et al.*, *Proc. Natl. Acad. Sci. U.S.A.* **101**, 101073/pnas.1503449112 (2015).
37. H. Jiang *et al.*, *Phys. Rev. Lett.* **110**, 205501 (2013).
38. C. Song *et al.*, *Phys. Rev. Lett.* **100**, 025504 (2008).
39. A. Tripathi *et al.*, *Proc. Natl. Acad. Sci. U.S.A.* **108**, 13393–13398 (2011).
40. D. A. Shapiro *et al.*, *Nat. Photonics* **8**, 765–769 (2014).
41. M. C. Newton, S. J. Leake, R. Harder, I. K. Robinson, *Nat. Mater.* **9**, 120–124 (2010).
42. M. D. Seaberg *et al.*, *Opt. Express* **19**, 22470–22479 (2011).
43. D. Shapiro *et al.*, *Proc. Natl. Acad. Sci. U.S.A.* **102**, 15343–15346 (2005).
44. H. Jiang *et al.*, *Proc. Natl. Acad. Sci. U.S.A.* **107**, 11234–11239 (2010).
45. J. Nelson *et al.*, *Proc. Natl. Acad. Sci. U.S.A.* **107**, 7235–7239 (2010).
46. Y. Nishino, Y. Takahashi, N. Imamoto, T. Ishikawa, K. Maeshima, *Phys. Rev. Lett.* **102**, 018101 (2009).
47. C. Song *et al.*, *Phys. Rev. Lett.* **101**, 158101 (2008).
48. H. Jiang *et al.*, *Phys. Rev. Lett.* **100**, 038103 (2008).
49. R. Neutze, R. Wouts, D. van der Spoel, E. Weckert, J. Hajdu, *Nature* **406**, 752–757 (2000).
50. T. Ekeberg *et al.*, *Phys. Rev. Lett.* **114**, 098102 (2015).
51. T. Kimura *et al.*, *Nat. Commun.* **5**, 3052 (2014).
52. M. Gallagher-Jones *et al.*, *Nat. Commun.* **5**, 3798 (2014).
53. M. F. Hantke *et al.*, *Nat. Photonics* **8**, 943–949 (2014).
54. H. N. Chapman *et al.*, *Nature* **470**, 73–77 (2011).
55. J. Tenboer *et al.*, *Science* **346**, 1242–1246 (2014).
56. J. Kern *et al.*, *Science* **340**, 491–495 (2013).
57. W. Liu *et al.*, *Science* **342**, 1521–1524 (2013).
58. A. Barty *et al.*, *Nat. Photonics* **2**, 415–419 (2008).
59. J.-D. Nicolas *et al.*, *J. Appl. Cryst.* **47**, 1596–1605 (2014).
60. J. Miao, K. O. Hodgson, D. Sayre, *Proc. Natl. Acad. Sci. U.S.A.* **98**, 6641–6645 (2001).
61. R. Fung, V. Shneerson, D. K. Saldin, A. Ourmazd, *Nat. Phys.* **5**, 64–67 (2009).
62. N.-T. D. Loh, V. Elser, *Phys. Rev. E Stat. Nonlin. Soft Matter Phys.* **80**, 026705 (2009).

## ACKNOWLEDGMENTS

We thank C. Pellegrini and J. M. Rodenburg for stimulating discussions and H. Jiang, J. Zhou, Y. Yang, and D. Adams for help with the figures and references. J.M. and M.M.M. acknowledge support from the Defense Advanced Research Projects Agency PULSE program through a grant from AMRDEC. J.M. thanks support from NSF (grant DMR-1437263). M.M.M. thanks support from NSF, DOE, and SRC. I.K.R. acknowledges support from an ERC “Advanced” grant. The University of Colorado and the University of Michigan have patents coauthored by M.M.M. in the area of high harmonic sources: U.S. Patent 8,462,824 (2013) and U.S. Patent 6151155 (2000).

## SUPPLEMENTARY MATERIALS

www.sciencemag.org/content/348/6234/530/suppl/DC1  
Supplementary Text  
References (63–92)

10.1126/science.aaa1394



## Beyond crystallography: Diffractive imaging using coherent x-ray light sources

Jianwei Miao *et al.*

*Science* **348**, 530 (2015);

DOI: 10.1126/science.aaa1394

*This copy is for your personal, non-commercial use only.*

If you wish to distribute this article to others, you can order high-quality copies for your colleagues, clients, or customers by [clicking here](#).

Permission to republish or repurpose articles or portions of articles can be obtained by following the guidelines [here](#).

**The following resources related to this article are available online at [www.sciencemag.org](http://www.sciencemag.org) (this information is current as of April 30, 2015):**

**Updated information and services**, including high-resolution figures, can be found in the online version of this article at:

<http://www.sciencemag.org/content/348/6234/530.full.html>

**Supporting Online Material** can be found at:

<http://www.sciencemag.org/content/suppl/2015/04/29/348.6234.530.DC1.html>

A list of selected additional articles on the Science Web sites **related to this article** can be found at:

<http://www.sciencemag.org/content/348/6234/530.full.html#related>

This article **cites 86 articles**, 13 of which can be accessed free:

<http://www.sciencemag.org/content/348/6234/530.full.html#ref-list-1>

This article appears in the following **subject collections**:

Physics

<http://www.sciencemag.org/cgi/collection/physics>